NEURAL REGENERATION RESEARCH
www.nrronline.org

Research Article

Characteristics of traumatic brain injury models: from macroscopic blood flow changes to microscopic mitochondrial changes

Ding-Ding Yang[1, #], Xiang-Dong Wan[1, 2, #], An-Di Chen[1, #], Zi-Qian Yan[1, 2], Yi-Fan Lu[1, 3], Jun-Chen Liu[1], Ya-Zhou Wang[1], Jing Wang[4], Yan Zhao[5, *], Sheng-Xi Wu[1, *], Guo-Hong Cai[1, 4, *]

https://doi.org/10.4103/1673-5374.369125

Date of submission: September 1, 2022

Date of decision: November 17, 2022

Date of acceptance: December 21, 2022

Date of web publication: March 3, 2023

From the Contents

Introduction	2268
Methods	2269
Results	2270
Discussion	2273

Graphical Abstract

Changes of cerebral blood flow and mitochondria in controlled cortical impingement models with different degrees of injury

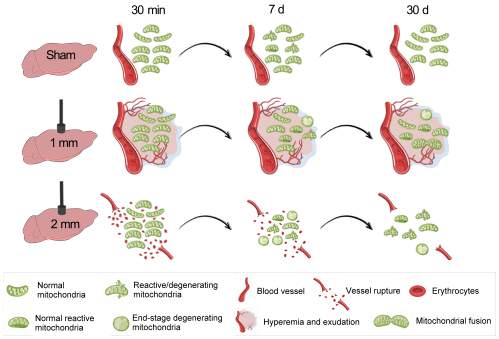

Abstract

Controlled cortical impingement is a widely accepted method to induce traumatic brain injury to establish a traumatic brain injury animal model. A strike depth of 1 mm at a certain speed is recommended for a moderate brain injury and a depth of > 2 mm is used to induce severe brain injury. However, the different effects and underlying mechanisms of these two model types have not been proven. This study investigated the changes in cerebral blood flow, differences in the degree of cortical damage, and differences in motor function under different injury parameters of 1 and 2 mm at injury speeds of 3, 4, and 5 m/s. We also explored the functional changes and mitochondrial damage between the 1 and 2 mm groups in the acute (7 days) and chronic phases (30 days). The results showed that the cerebral blood flow in the injured area of the 1 mm group was significantly increased, and swelling and bulging of brain tissue, increased vascular permeability, and large-scale exudation occurred. In the 2 mm group, the main pathological changes were decreased cerebral blood flow, brain tissue loss, and cerebral vasospasm occlusion in the injured area. Substantial motor and cognitive impairments were found on day 7 after injury in the 2 mm group; at 30 days after injury, the motor function of the 2 mm group mice recovered significantly while cognitive impairment persisted. Transcriptome sequencing showed that compared with the 1 mm group, the 2 mm group expressed more ferroptosis-related genes. Morphological changes of mitochondria in the two groups on days 7 and 30 using transmission electron microscopy revealed that on day 7, the mitochondria in both groups shrank and the vacuoles became larger; on day 30, the mitochondria in the 1 mm group became larger, and the vacuoles in the 2 mm group remained enlarged. By analyzing the proportion of mitochondrial subgroups in different groups, we found that the model mice had different patterns of mitochondrial composition at different time periods, suggesting that the difference in the degree of damage among traumatic brain injury groups may reflect the mitochondrial changes. Taken together, differences in mitochondrial morphology and function between the 1 and 2 mm groups provide a new direction for the accurate classification of traumatic brain injury. Our results provide reliable data support and evaluation methods for promoting the establishment of standard mouse controlled cortical impingement model guidelines.

Key Words: cerebral blood flow; cognitive impairments; controlled cortical impingement; ferroptosis; mitochondrial dysfunction; motor impairments; mouse model; traumatic brain injury

Introduction

Traumatic brain injury (TBI) is a major health problem worldwide (Dewan et al., 2018). TBI is the main cause of death and disability among all trauma-related injuries globally (Rubiano et al., 2015; Majdan et al., 2016; Moore et al., 2020). Several studies have shown that craniocerebral injury can promote the development of degenerative diseases (Bagnato and Boccagni, 2020). Furthermore, TBI has a significant impact on a patient's cognition and mood (Muresanu et al., 2022) and is a high-risk factor for cerebral hemorrhage, cerebral infarction, cerebral vasospasm, and epilepsy (Al-Mufti et al., 2017; Chen et al., 2022; Karlander et al., 2022).

Several TBI animal models have been established. The controlled cortical impingement (CCI) model has a high reproducibility rate and can better simulate brain tissue contusion, cortical tissue loss, and post-traumatic epilepsy after TBI, compared with models established by other methods, such

[1]Department of Neurobiology, School of Basic Medicine, Forth Military Medical University, Xi'an, Shaanxi Province, China; [2]Hebei Medical University, Shijiazhuang, Hebei Province, China; [3]College of Life Sciences & Research Center for Resource Peptide Drugs, Yan'an University, Yan'an, Shaanxi Province, China; [4]Department of Nuclear Medicine, First Affiliated Hospital of Forth Military Medical University, Xi'an, Shaanxi Province, China; [5]Department of Gastroenterology, First Affiliated Hospital of Xi'an Jiaotong University, Xi'an, Shaanxi Province, China

*Correspondence to: Guo-Hong Cai, PhD, guohong_neuron@163.com; Sheng-Xi Wu, PhD, shengxi@fmmu.edu.cn; Yan Zhao, MD, yanzhao211@163.com.
https://orcid.org/0000-0001-7511-7420 (Guo-Hong Cai); https://orcid.org/0000-0002-3210-9567 (Sheng-Xi Wu); https://orcid.org/0000-0002-0638-4741 (Yan Zhao)
#These authors contributed equally to this work.

Funding: *This work was supported by grants from the National Science and Technology Innovation 2030 Grant of China, No. 2021ZD0201005 (to SXW); Natural Science Foundation of China, Nos. 81900489 (to YZ), 82101294 (to GHC), 81730035 (to SXW), Natural Science Foundation of Shaanxi Province, No. 2022JM-456 (to YZ); Shaanxi Provincial Key Research and Development Program, Nos. 2022SF-011 (to GHC), 2022ZDLSF01-02 (to YZW).*

How to cite this article: *Yang DD, Wan XD, Chen AD, Yan ZQ, Lu YF, Liu JC, Wang YZ, Wang J, Zhao Y, Wu SX, Cai GH (2023) Characteristics of traumatic brain injury models: from macroscopic blood flow changes to microscopic mitochondrial changes. Neural Regen Res 18(10):2268-2277.*

as weight-drop method (Siebold et al., 2018; Wang et al., 2021). The mouse CCI model is currently the most widely studied animal model of TBI and is a resource for pathological mechanism research and drug target development with knockout and transgenic technology (Zhang et al., 2014). The CCI model is a model that uses the strike instrument to strike the animal brain under the target parameters (injury depth, injury speed, and dwell time) (Yang et al., 2021). Different modeling parameters determine the degree of animal injury. However, there is no clear classification of TBI models (Siebold et al., 2018). Siebold et al. (2018) reviewed 58 CCI mouse model studies in relation to modeling parameters and injury degree. The study recommended specific injury parameters: mild: no craniotomy, cortical depression < 0.5 mm, speed < 4.0 m/s; moderate: craniotomy, cortical depression 1.0–1.5 mm, speed 4.0–5.0 m/s; severe: craniotomy, cortical depression > 2.0 mm, speed > 5.0 m/s. To establish a model with mild injuries, a model without craniotomy is recommended to simulate a concussion-type injury. However, the specific guidelines for the injury parameters for moderate and severe injuries are not well defined, and the lack of consensus regarding CCI modeling in mice has resulted in considerable variability between laboratories and studies.

TBI is caused by deformations of brain tissue induced by mechanical force. Almost all severe TBI patients have damage to blood vessels (Jullienne et al., 2016); the rupture and spasm of blood vessels can disrupt the homeostasis of the central nervous system and expose nervous tissue to injury (Hu and Tao, 2021). Even abnormal changes in cerebral hemodynamics will affect the function of the entire brain (Zheng et al., 2022). The mouse skull is thin and translucent; thus, mice are a good model to examine the changes in cerebral surface hemodynamics after craniocerebral injury.

In this study, to explore the different injury parameters for CCI modeling of moderate and severe injury, we examined the effects and underlying mechanisms between the 1 and 2 mm impingement models in mice. We evaluated the hemodynamic, morphological, and behavioral changes of the 1 and the 2 mm groups at different injury speeds. We further examined the 1 and 2 mm groups in the acute and chronic phases. Following results in the literature, we selected days 7 and 30 after trauma as the acute and chronic observation points, respectively. We studied animal gait, cognition, and mitochondrial-related indicators in the 1 and 2 mm groups on days 7 and 30. These findings will provide evidence to help inform the establishment of CCI models.

Methods

Animals

To exclude the influence of sex hormones, only adult male mice were included in this study. Adult male C57BL mice (aged 6–7 weeks, approximately 20 g, *n* = 150) were obtained from the Animal Center of the Air Force Medical University (Fourth Military Medical University), Xi'an, China (license No. SCXK (Shaan) 2019-001). The mice were maintained in a specific pathogen-free level environment, with five or six mice housed in each cage, with an ambient temperature of 25°C. Animals were housed in humidity-controlled (50% relative humidity) conditions with a 12-hour light/dark cycle. The mice had *ad libitum* access to food and water. All procedures followed the Air Force Medical University's ethical guidelines for the care and use of laboratory animals. The animal experimental protocol was approved by the Animal Care and Use Committee of the Air Force Military Medical University (approval No. IACUC-20220175, approval date: January 15, 2021).

TBI surgery

To establish the CCI model, mice were injected intraperitoneally with 1% sodium pentobarbital (11715, Sigma, St. Louis, MO, USA) (60 mg/kg) and placed in a standard brain stereotaxic apparatus (68507, RWD Life Science Co., Ltd., Shenzhen, China). After iodine phenol disinfection, a 2 cm incision was made along the midline of the mouse scalp. Each layer of tissue was dissociated to expose the skull. A 0.5 cm diameter bone window was made with a dental drill 0.5 cm to the right and 0.5 cm posterior to the Bregma point. The strike center was 1.5 mm to the right and –1.8 mm posterior to the Bregma point in accordance with the brain atlas (Paxinos and Franklin, 2013). CCI was performed using a precision impact device (68099II, RWD Life Science Co., Ltd.; **Figure 1A**). Modeling was carried out following different striking parameters with a contact time of 500 ms. Care was taken to ensure the integrity of the dura mater during surgery, since the impact device uses electrical conduction to determine the plane where the dura mater is located. To avoid human error, physiological saline was used to keep the impacted area moist during the operation. To avoid the influence of the liquid surface tension caused by excessive liquid residue, the critical surface was aligned before it was hit and the target area was parallel to the plane of the hitting head. After the injury, the bleeding was stopped with gel foam and the incision was sutured. The operations were performed by a single person to avoid operator error.

The sham group underwent surgery and anesthesia. After recovery from CCI injury, all mice were returned to their cages.

The allotment of animals for analysis was as follows:
(1) For cerebral blood flow index monitoring, gelatin fluorescein isothiocyanate (FITC)-labeled blood vessels, and hematoxylin and eosin staining, mice were randomly divided into seven groups (*n* = 3 per group): the sham group and the TBI groups (1 mm (3 m/s), 2 mm (3 m/s), 1 mm (4 m/s), 2 mm (4 m/s), 1 mm (5 m/s), and 2 mm (5 m/s)).
(2) For CatWalk XT® analysis, mice were randomly divided into seven groups (*n* = 8 per group): the sham group and the TBI groups (1 mm (3 m/s), 2 mm (3 m/s), 1 mm (4 m/s), 2 mm (4 m/s), 1 mm (5 m/s), and 2 mm (5 m/s)).
(3) For the rotarod test, mice were randomly divided into seven groups (*n* = 6 per group): the sham group and the TBI groups (1 mm (3 m/s), 2 mm (3 m/s), 1 mm (4 m/s), 2 mm (4 m/s), 1 mm (5 m/s), and 2 mm (5 m/s).
(4) For the new object recognition test, the mice were randomly divided into three groups (*n* = 6 per group): the sham group and the TBI groups (1 mm (5 m/s) and 2 mm (5 m/s)).
(5) For RNA-Seq, mice were randomly divided into three groups (*n* = 5 per group): the sham group and the TBI groups (1 mm (5 m/s) and 2 mm (5 m/s) at 30 days after CCI).
(6) For lipid peroxidation assay and Perl's iron staining and reactive oxygen species (ROS) chemifluorescence assay, mice were randomly divided into three groups (*n* = 3 per group): the sham group and the TBI groups (1 mm (5 m/s) and 2 mm (5 m/s) at 30 days after CCI).
(7) For transmission electron microscope and mitochondrial complex assay, mice were randomly divided into six groups (*n* = 3 per group): the sham and the TBI groups (1 mm (5 m/s) and 2 mm (5 m/s) at 7 days after CCI) and the sham and TBI groups (1 mm (5 m/s) and 2 mm (5m/s) at 30 days after CCI).

Cerebral blood flow index monitoring

The skull was exposed and placed under laser-speckle contrast imaging for 10 minutes of baseline video before the injury, and laser-speckle contrast imaging monitoring was performed for 30 minutes immediately after the injury. The laser-speckle contrast imaging system (National Laboratory for Optoelectronics, Wuhan, China) consists of an Olympus ZS61 microscope, a continuous-wavelength laser diode (*k* = 785 nm), a charge-coupled device camera, and a computer. The observation area was illuminated by a continuous wavelength laser light source. Speckle signals were continuously acquired by a camera (10 minutes exposure time) and then transferred to a computer for analysis. The region of interest (ROI) was selected using the computer software (SIM BFI Software, National Laboratory for Optoelectronics, Wuhan, China), and the obtained value was the average cerebral blood flow index (BFI) of the region in perfusion units (U). Three regions of interest were chosen (**Figure 1B**), with the cerebral blood flow before the strike as the baseline. Absolute value representations of BFI were obtained in each region of interest. The BFI was recorded in the damaged area, the same side of the damaged area, and the opposite side of the damaged area before the injury and 10, 20, and 30 minutes after CCI. The experimental process is shown in **Figure 1C**.

Gelatin FITC-labeled blood vessels

Mice were anesthetized by intraperitoneal injection of 1% sodium pentobarbital at a dose of 80 mg/kg. The mice were then fixed on the dissection table and the thoracic cavity was opened to expose the heart. An injection needle was pinched by hand and inserted into the apex of the heart. The needle position was fixed and the atrial appendage of the right atrium was cut with scissors. The constant flow pump was turned on and perfusion with 0.01 M phosphate-buffered saline, approximately 30 mL, was performed. Next, 30 mL of 4% paraformaldehyde (PFA) (P6148, Sigma) was perfused, followed by perfusion of 0.03% (w/v) gelatin FITC (YF9121, Bomei, Hefei, China) at 40°C while keeping the mouse head down and pouring approximately 30 mL of hot gelatin FITC. The head was immediately placed in ice water 30 minutes. The head was then decapitated, the skin was peeled off (with care not to squeeze the head too hard to avoid deformation of blood vessels), and the remaining head was placed in 4% PFA overnight. The next day, the skull was opened to remove the brain, taking care not to damage the blood vessels on the surface of the brain. The brain was separated and harvested, and the brain was peeled off into a culture flask filled with 4% PFA and held at 4°C for 24 hours. Sections were sliced to a thickness of 50 μm using an oscillating microtome (VT1200S, Leica, Hessian, Germany) and photographed with a fluorescence microscope (BX51WI, Olympus, Tokyo, Japan).

Gait analysis

The CatWalkXT® version 10.6 automatic gait analysis system (Nordus Information Technology, Wageningen, The Netherlands) consists of a walkway (a 1.3 m horizontal glass panel) covered by a tunnel. Animals were placed at one end of the walkway and allowed to walk across the panel through the tunnel to a cage. Green LED light is emitted and reflected inside the glass panel, and any areas of contact with the glass panel (footprints) are detected by a camera. Captured data is analyzed automatically by the CatWalkXT® software. Data on paw print area, paw strength, base of support hind paws, and other indicators are captured. After initial acclimatization to the new environment, animals must perform at least three uninterrupted runs to qualify for gait analysis. For calibration parameters, the maximum speed change was 60%, the camera gain was 16.99 dB, and the detection threshold was 0.1 a.u.

Hematoxylin and eosin staining and analysis

At 24 hours after TBI, four mice in each group were anesthetized by intraperitoneal injection of 1% sodium pentobarbital at a dose of 80 mg/kg; the chest cavity was opened, and the right atrial appendage was cut through left ventricular puncture. The blood was flushed with normal saline; fixation was performed by perfusion with phosphate buffer containing 4% PFA, and dehydration was performed using 30% sucrose. The brain was then embedded in Optimal Cutting Temperature (OCT) and serially sectioned at a thickness of 20 μm for hematoxylin and eosin staining. Images were obtained, and the thickness of the cortical swelling, the depth of the cortical defect,

and the area of cortical hemorrhage were measured using ImageJ software (version 1.8.0, National Institutes of Health, Bethesda, MD, USA; Schneider et al., 2012).

Rotarod test

The rotarod test was used to evaluate the motor coordination of mice (ZB-200, Chengdu Taimeng Software Co., Ltd., Fujian, China). Rotarod training was initiated on the fourth day after TBI. The mice were trained for 3 days, three times a day. The interval between each training session was 10 minutes, and the rotarod speed was 40 r/min. Experiments were performed on day 7 after TBI, and the falling time of mice at a rotating rod speed of 40 r/min was recorded. If the mouse did not fall within 180 seconds, the latency time was counted as 180 seconds. The average value of three recordings was calculated.

New object recognition and data analysis

The new object recognition test box was 50 cm × 50 cm × 20 cm; the side walls and bottom surfaces were made of white opaque materials. The first day was the adaptation period, in which mice were put into the experimental box to adapt for 10 minutes; the second day was the familiarization period, in which two identical yellow spherical blocks were placed on the diagonal of the test box, and the mice were placed with their backs to the blocks and allowed to explore the test box for 10 minutes. After 6 hours, the test period was initiated; one of the spherical blocks was replaced with a purple square box; the mice were placed in the test box with their backs to the building block, and they were free to explore for 10 minutes. The time spent exploring the old and new objects during the test period was recorded. The discrimination index was calculated as:

Discrimination index = total time to explore new objects / (total time to explore new objects + total time to explore old objects)

After each mouse was tested, any feces and urine in the box was cleaned using 75% alcohol to eliminate odors. After the test, each mouse was placed in a new cage. The experimenter kept quiet and kept away from the test mice during the whole process. The video acquisition and storage system was purchased from DongLe Natural Gene Life Science Company (Beijing, China) and Smart3.0 behavior analysis software was used (Panlab, Barcelona, Spain).

RNA extraction, library construction, and sequencing

Total RNA was extracted from injured areas of brain tissues using the Trizol reagent kit (Invitrogen, Carlsbad, CA, USA) following the manufacturer's protocol. RNA quality was assessed on an Agilent 2100 Bioanalyzer (Agilent Technologies, Palo Alto, CA, USA) and checked by RNase-free agarose gel electrophoresis (A6013, Sigma). After total RNA was extracted, eukaryotic mRNA was enriched by Oligo (dT) beads. The enriched mRNA was fragmented into short fragments using fragmentation buffer and reverse transcribed into cDNA (NEBNext Ultra RNA Library Prep Kit for Illumina, NEB# 7530, New England Biolabs, Ipswich, MA, USA) with random primers. Second-strand cDNA was synthesized by DNA polymerase I, RNase H, dNTP, and buffer (NEB# 7530, New England Biolabs). The cDNA fragments were purified with a QiaQuick PCR extraction kit (Qiagen, Venlo, The Netherlands), end repaired, poly(A) added, and ligated to Illumina sequencing adapters. The ligation products were size-selected by agarose gel electrophoresis, PCR amplified, and sequenced using Illumina Novaseq6000 by Gene Denovo Biotechnology Co. (Guangzhou, China).

Differentially expressed genes (DEGs) were assessed by analysis of differential RNA expression between two groups. Transcripts with false discovery rate below 0.05 and an absolute fold change of 2 or greater were considered differentially expressed. We performed gene set enrichment analysis using Gene Set Enrichment Analysis (GSEA, 4.3.0) and Molecular Signatures Database (Mouse MSigDB, v2022.1.Mm) and examined significant differences in Gene Ontology (GO) terms and Kyoto Encyclopedia of Genes and Genomes (KEGG) pathways between groups. Briefly, we input gene expression matrix and ranked genes by the SinaltoNoise normalization method. Enrichment scores and *p* value were calculated in default parameters. *P* values below 0.05 and absolute normal enrichment scores (NES) ≥ 1 indicated a significant enrichment pathway or GO term. The RNA-Seq data used in this study have been deposited in the NCBI's Sequence Read Archive (SRA) (SRA study accession code, SUB11975733; https://www.ncbi.nlm.nih.gov/sra/PRJNA874212).

Lipid peroxidation assay

Lipid peroxidation was determined using the lipid peroxidation malondialdehyde (MDA) detection kit (S0131, Beyotime, Shanghai, China), in which MDA produced in the cortex reacts with thiobarbituric acid (TBA) to form a red MDA-TBA complex, which is quantified using a spectrophotometer (SpectraMax iD3, Molecular Devices, Shanghai, China) at 532 nm. The damaged cortical tissue in mice 30 days after CCI was homogenized, mixed with MDA working solution, and heated in boiling water for 15 minutes. After cooling, the supernatant was centrifuged and absorbance at 532 nm was determined.

Perl's iron staining

Brain tissues from injured areas were placed in Perl's staining solution from the Beijing Solarbio Prussian Blue Staining Kit (G1428, Solarbio, Beijing, China) and incubated at 37°C for 20 minutes. After washing, the tissues were incubated at 37°C for 20 minutes. Tissues were washed and incubated in enhanced working solution for 20 minutes, dehydrated, and sealed. The brown-yellow stained area and integrated optical density were measured by ImageJ.

Transmission electron microscopy

Mice were anesthetized and perfused with 0.01 M phosphate-buffered saline, 2% formaldehyde, and 2% glutaraldehyde in sequence. Approximately 1 mm^3 of brain tissue injury area was removed and placed in 2.5% glutaraldehyde for tissue fixation. Samples were washed three times with 0.1 M PBS followed by staining in 1% osmic acid (18466, Tedpella, CA, USA) for 2 hours. The samples were rinsed three times with deionized water and dehydrated with 50%, 70%, and 90% ethanol and 100% acetone; the tissue block was infiltrated with acetone:embedding medium (SPI-02660, SPI, PA, USA) in a 1:1 ratio. Embedding and polymerizing was performed at 60°C overnight and 70-nm-thick sections were prepared using an ultramicrotome (Leica EM UC7, Leica, Hessian, Germany). Sections were placed on copper grids and stained with lead nitrate (Kermel, Tianjin, China) and uranyl acetate (SPI Supplies, West Chester, PA, USA) for 10 minutes. Images were recorded using a transmission electron microscope (JEM1400, Olympus). Morphology of mitochondria and vacuoles were analyzed using ImageJ.

Morphometric analysis

The size of each mitochondrion was obtained by drawing the electron microscopy sagittal profile of the mitochondria in the brain damage area. The scale was set using the bar of the picture in ImageJ. With the freehand selections of the software, the outline of mitochondria was carefully drawn, and the perimeter and area of the mitochondria were measured. Roundness calculations were performed on the basis of the measured mitochondrial area and perimeter as follows: circularity = $4\pi \times \text{area } (\mu m^2)/\text{perimeter } (\mu m)^2$. The number of mitochondria in the brain damage area in each image were manually counted to obtain the total number of mitochondria the density of mitochondria was determined. The same methods were used to calculate the area and perimeter of the vacuoles in the mitochondria. We also calculated the ratio of the sum of the area of all vacuoles in a single mitochondrion to the total area of the mitochondria.

Mitochondrial complex assay

The activities of mitochondrial complexes I–V were monitored using detection kits (Cat# BC0515, BC3240, BC0945, BC1445, BC3235, Solarbio Life Sciences, Beijing, China). Briefly, approximately 0.1 g of brain tissue was taken from the injured area; mitochondrial extraction solution was used for mitochondrial extraction, and the extracted mitochondria were subjected to ultrasonic disruption (power 20%, ultrasonic for 5 seconds, interval of 10 seconds, 15 times). According to the functions of different mitochondrial complexes, the samples were added to the corresponding working solution, and the spectrophotometric value was measured after incubation for a certain time period; the activities of different mitochondrial complexes were calculated following the manufacturer's instructions.

ROS assay

An active oxygen chemical fluorescence assay kit (E004-1-1, Jiancheng, Nanjing, China) was used for ROS assays. Briefly, approximately 0.1 g of sample was taken from the damaged area and ground into a single cell suspension. The diacetyldichlorofluorescein probe was added and the sample was incubated for 1 hour in the dark. The diacetyldichlorofluorescein probe passes through the cell membrane and hydrolyzes to DCFH. When ROS is present in a cell, DCFH is oxidized to a strong green color. A microplate reader (SpectraMax iD3, Molecular Devices, Shanghai, China) was used to evaluate readings at 500 nm fluorescence excitation.

Statistical analysis

No statistical methods were used to predetermine sample sizes; however, our sample sizes are similar to those reported in previous publications (Fischer et al., 2016; Hubbard et al., 2019; Walter et al., 2022). Data are presented as mean ± standard error (SEM). Statistical analysis was performed using SPSS 19.0 (IBM Corp., Armonk, NY, USA). Statistical analysis was conducted by researchers blinded to the experimental design. For comparison of two groups that conformed to the normal distribution and homogeneity of variance, the two tailed unpaired *t*-test was used; otherwise, Mann-Whitney *U* test was used. For comparison of more than two groups that conformed to normal distribution and homogeneity of variance, one-way analysis of variance followed by Tukey's multiple comparisons test was used; otherwise Kruskal-Wallis *H* test and Nemenyi multiple comparisons test was used. Repeated measurement analysis of variance followed by Student-Newman-Keuls test was adopted when the data conformed to repeated measurement design (cerebral blood flow detection) and normal distribution and homogeneity of variance; otherwise, Friedman's *M* test and Student-Newman-Keuls test were adopted. *P* value < 0.05 indicated statistical significance. See **Additional Tables 1** and **2** for details.

Results

Impact of strike depth and strike speed on tissue damage

We first examined differences in cerebral surface blood flow changes in six groups of CCI model mice (1 and 2 mm at speeds of 3, 4, and 5 m/s). We performed blood flow imaging within 30 minutes after injury. Three regions were selected on the brain surface for the dynamic observation of blood perfusion. We found that there was a different trend of blood flow changes in the brain injury area between the 1 and 2 mm groups. In the 1 mm group,

the cerebral blood perfusion index increased at first and then tended to flatten within 30 minutes; in the 2 mm group, the cerebral blood perfusion index showed a significant downward trend within 30 minutes (**Figure 1D** and **E**). The phenomenon was observed within the first 10 minutes (**Figure 1F**) and persisted until 24 hours after injury (**Additional Figure 1A**). To observe the changes of blood flow distribution in the whole brain after injury, we performed blood flow detection on both the ipsilateral and contralateral area of the injured brain 30 minutes after injury (**Additional Figure 1B**); the blood flow in these areas decreased to varying degrees after injury (**Figure 1G–J**). This reflects the dynamic changes of blood perfusion in the injured area and the ipsilateral and contralateral brain areas within 30 minutes after the injury. Taken together, our results suggest that the hemodynamic effects of CCI are brain-wide. This result is consistent with the decreased cerebral blood flow observed in patients with clinical TBI (Anania et al., 2021).

Many factors affect blood perfusion. To further examine the vascular injury under different parameters, we performed whole-brain vascular gelatin-FITC perfusion imaging immediately after injury (**Figure 2A** and **F–K**). We observed that changes in cortical blood vessels in the injured area of mice in the 1 mm group were mainly exudative in nature, and the vascular permeability was increased, resulting in leakage of gelatin. The blood vessels around the injured area were arranged in a disorderly fashion, and the brain tissue was relatively intact. In the 2 mm group, there was occlusion of blood vessels in the injured area and irregular dark areas, while the brain tissue around the injury area showed congestion and exudation.

To further examine the effect of vascular changes on the pathology of brain tissue, we performed hematoxylin and eosin staining on brain tissues within 24 hours after injury (**Figure 2A**, **2F–K**) and evaluated the thickness of brain tissue swelling in the 1 mm group and the depth of brain tissue loss in the 2 mm group. The subcortical hemorrhage area was manually delineated and analyzed. We found that the swelling thickness of the brain tissue (**Figure 2B**) and the subcortical hemorrhage area in the 1 mm group increased with the increase of the injury speed (**Figure 2C**). Additionally, the increase in velocity led to an increase in the depth of cortical loss (**Figure 2D**) and the area of subcortical hemorrhage in the 2 mm group (**Figure 2E**). These results suggest that 1 and 2 mm strike depths cause two different damage patterns; the 1 mm striking depth led to increased blood flow in the injured area, while the 2 mm striking depth resulted in decreased blood flow in the injured area. Additionally, the effect of speed on the injury outcome varied in accordance with the different degree of the two types of injury.

There is a marked difference in dyskinesia between the 1 and 2 mm groups on day 7 after injury

Gait analysis (**Figure 3A**) is an objective tool to assess motor function in CCI model mice (Walter et al., 2020). We performed gait analysis by examining static indicators such as paw print area and paw strength-related indicators and dynamic indicators such as swing speed, duty cycle, body speed, and swing (**Figure 3B**). We found significant differences in static parameters between the 1 mm and 2 mm groups (**Figure 3C**). There were also differences in body speed and other measures (**Additional Figures 2–10**). Therefore, we used the paw printing area and average paw strength as the main reference indicators. The results showed that the exercise ability of the limbs of the mice in the 2 mm group was affected to different degrees (**Figure 3D** and **E**). The results of the rotarod experiment (**Figure 3F**) indicated that the latency to fall in mice in the 1 and 2 mm groups was not significantly different from the sham group when the speed was 3 m/s (**Figure 3G**). However, the latency to fall in the 1 and 2 mm groups was significantly shorter than that of the sham group when the speed was 4 and 5 m/s (4 m/s: $P_{sham\text{-}1mm}$= 0.0037; $P_{sham\text{-}2mm}$= 0.0013; 5 m/s: $P_{sham\text{-}1mm}$=0.0068; $P_{sham\text{-}2mm}$= 0.0017; **Figure 3H** and **I**). However, these differences disappeared on day 30 (**Figure 4A–G**).

Motor dysfunction in the 2 mm group recovers on day 30 but cognitive impairment persists

We continued to observe the 5 m/s groups and performed rotarod and gait analysis on day 30 (**Figure 4A**). In the rotarod experiment, the functional defects of the 1 and 2 mm groups observed on day 7 were recovered by day 30, but the 2 mm group had not fully recovered to normal (**Figure 4B**). To exclude the effect of body weight on exercise ability (Pitzer et al., 2021), we evaluated the body weight on days 7 and 30 after injury; there was no difference between groups, and all groups exhibited a significant body weight increase (**Figure 4C**). After 30 days of recovery, the difference in gait between the 1 and 2 mm groups disappeared (**Figure 4D–G** and **Additional Figure 11**).

Cognitive dysfunction is often reported after TBI. We thus next tested the ability of mice to recognize new objects on days 7 and 30 after CCI. We found that cognitive impairment after TBI in the 2 mm group persisted on day 30, and a difference between the 1 and 2 mm groups was observed (**Figure 4H** and **I**). Pathology revealed small amounts of liquefaction and necrosis in the brain tissue of the 1 mm group on day 30, but the overall shape of the brain tissue was intact and there was no obvious deformation. However, in the 2 mm group, we observed a loss of brain tissue in the injured area, obvious atrophy of the brain tissue on the injured side, deviation of the midline structures of the brain, and significant deformation of the brain morphology (**Figure 4J**). These results showed that cognitive impairment is one of the manifestations of chronic phase.

Identification of DEGs in the injured area of the three groups of mouse models of traumatic brain injury on day 30

From the above results, we found marked differences between the 1 and 2 mm groups in histopathology and behavior. To further explore the pathological mechanism that leads to the macroscopic difference between 1 and 2 mm groups, we detected the changes of gene transcriptome in the damaged regions of sham, 1 mm (5 m/s) and 2 mm (5 m/s) mice. The results revealed 221 DEGs in the 1 mm group compared with the sham group, including 200 up-regulated DEGs and 21 down-regulated DEGs (**Figure 5A** and **B**), and 1441 DEGs in the 2 mm group, including 1404 up-regulated DEGs and 37 down-regulated DEGs (**Figure 5A** and **C**). We also identified 582 DEGs in the 2 mm group compared with the 1 mm group, including 571 up-regulated DEGs and 11 down-regulated DEGs (**Figure 5A** and **D**). GSEA showed that compared with the sham group, the first 10 items enriched in the 1 and 2 mm groups had the most mitochondrial-related function items, so we concluded that mitochondrial damage was very important in the CCI model. The top 10 gene sets for mitochondrial-related gene enrichment in the 1 and 2 mm groups are shown in **Figure 5E** and **F**. Mitochondrial respiratory chain-related genes were significantly decreased in both groups, mainly in the mitochondrial proton transport ATP synthase complex (mitochondrial respiratory chain complex V), and the expression of mitochondrial respiratory chain complex I-related genes decreased. Detailed Reactome enrichment analysis results are presented in the **Additional Figure 12**. We examined mitochondrial complex activity in the injury models on day 30 and found that mitochondrial respiratory chain complex V was significantly defective in the 2 mm group (**Figure 5G**); a reduction in mitochondrial respiratory chain complex activity in the 2 mm group was observed on day 7 (**Figure 5H**). Among the above differential genes, we found a significant decrease in the expression of mitochondrial respiratory chain complex-related genes in both the 1 and 2 mm groups compared with the sham group (**Figure 6A** and **B**). No differences in mitochondrial respiratory chain complex-related genes were found between the 1 and 2 mm groups (**Figure 6C**). This is consistent with the mitochondrial complex activity assay results (**Figure 5G**).

Higher numbers of ferroptosis-related DEGs are observed in the 2 mm group compared with the 1 mm group

Multiple studies have reported ferroptosis after CCI (Xie et al., 2018; Geng et al., 2021; Cheng et al., 2022). Thus, we next analyzed ferroptosis-related genes. We found that both the 1 and 2 mm groups had high expression of ferroptosis-related genes compared with the sham group (**Figure 6D** and **E**). Ferroptosis-related gene expression in the 2 mm group was significantly higher than that in the 1 mm group (**Figure 6F**). We further performed Perl's iron staining (**Additional Figure 13A–C**) and MDA assays (**Additional Figure 13D**). The results confirmed significant differences in iron deposition and lipid peroxidation in the 1 and 2 mm groups compared with the sham group.

Mitochondrial morphological changes in the injured area of the 1 and 2 mm groups on days 7 and 30

Mitochondria are involved in the occurrence and development of various neurological diseases, especially in hypoxic and ischemic environments (Hakiminia et al., 2022). Transcriptome sequencing revealed significant differences in mitochondrial dysfunction between the 1 mm group and the 2 mm group.

We examined brain tissue of the 1 mm and 2 mm groups on days 7 (**Figure 7A**) and 30 (**Figure 8A**) using transmission electron microscopy. We found reductions in mitochondrial area and circumference on day 7 in both the 1 and 2 mm groups (**Figure 7B** and **C**). However, the circularity of mitochondria has not changed significantly (**Figure 7D**). This is consistent with the changes of mitochondrial-related genes indicated by transcriptome sequencing after TBI. Additionally, the area and circumference of vacuoles inside the mitochondria in the 1 and 2 mm groups were significantly larger than those in the sham group (area: $P_{sham\text{-}1mm}$ = 0.032; $P_{sham\text{-}2mm}$ < 0.0001; circumference: $P_{sham\text{-}1mm}$ = 0.024; $P_{sham\text{-}2mm}$ < 0.0001), and the ratio of vacuole/mitochondria area in the 2 mm group increased significantly ($P_{sham\text{-}2mm}$ < 0.0001; **Figure 7E–G**), indicating that mitochondria have a large number of vacuoles. On day 30, the mitochondria in the 1 mm group were enlarged (**Figure 8B** and **C**), while the mitochondria in the 2 mm group became round (**Figure 8D**) and the vacuole area, circumferencethe and vacuole/mitochondria area ratio increased (**Figure 8E–G**). This indicated that the mitochondria in the 1 mm group showed a trend of fusion on day 30, while mitochondrial damage persisted in the 2 mm group. The mitochondrial changes in the 1 and 2 mm groups are listed in **Additional Table 3**.

We also examined the ROS content in the injured area of the brain tissue in the 1 and 2 mm groups on day 7; both groups exhibited a significant increase in ROS (**Additional Figure 14B**). Comparison of the ROS content with the gait analysis results revealed that base of support hind paws and ROS showed a significant negative correlation (**Additional Figure 14A–C**).

Proportion of mitochondrial subtypes in brain tissue in the 1 and 2 mm groups on days 7 and 30

Understanding the patterns of mitochondrial morphodynamic changes can help the evaluation of changes in cytoplasmic homeostasis as well as the subcellular pathologies of cell death (Balan et al., 2013). We divided the mitochondria into four types on the basis of microscopic morphology of the mitochondria in brain tissue after TBI (Balan et al., 2013): normal mitochondria, normal reactive mitochondria, reactive/degenerated mitochondria, and end-stage degenerating mitochondria. Changes in mitochondrial ultrastructure reflect overall severity of TBI, and levels of irreversible (end-stage degenerating) and reversible (normal reactive) mitochondrial changes reflect regional levels of brain injury severity. We

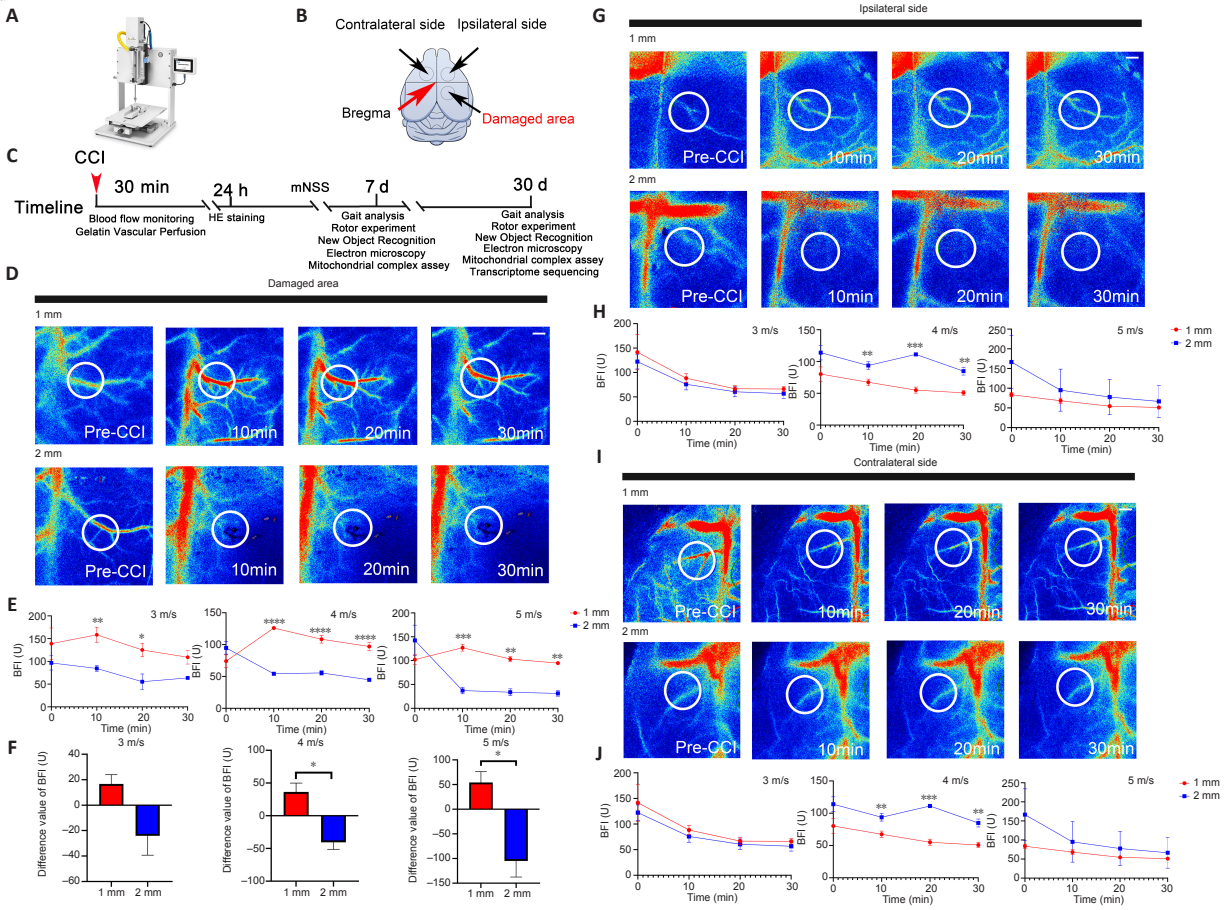

Figure 1 | **Changes of cerebral blood perfusion within 30 minutes of CCI model establishment detected by laser speckle imaging.**
(A) Schematic diagram of the equipment used in CCI modeling. (B) Schematic diagram of the injury area, region ipsilateral to the injury area, and region contralateral to the injury area. (C) Timeline of the mouse CCI modeling and experimental workflow. (D) Representative images of BFI changes in the damaged area 10, 20, and 30 minutes after injury. The white circle indicates the main detection range. (E) Statistical analysis of BFI changes in the damaged area 10, 20, and 30 minutes after injury (n = 3 mice in each group). (F) Changes of blood flow in the injured area 10 minutes after injury compared with the baseline (cerebral blood flow before injury) (n = 3 mice in each group). (G) Representative images of BFI changes 10, 20, and 30 minutes after injury ipsilateral to the injury area. The white circle is the main detection range. (H) Statistical analysis of BFI changes in the area on ipsilateral to the injury area, 10, 20, and 30 minutes after injury (n = 3 mice in each group). (I) Representative images of BFI changes 10, 20, and 30 minutes after injury in the area on contralateral to the injury area. The white circle indicates the main detection range. (J) Statistical analysis of BFI changes in the area on contralateral to the injury area 10, 20, and 30 minutes after injury. n = 3 mice in each group. Data are presented as mean ± SEM. $^*P < 0.05$, $^{**}P < 0.01$, $^{***}P < 0.001$, $^{****}P < 0.0001$ (repeated measures analysis of variance for E, H, J; two-tailed unpaired t-test for F). BFI: Blood flow index; CCI: controlled cortical impingement; HE: hematoxylin and eosin; mNSS: modified neurological severity score.

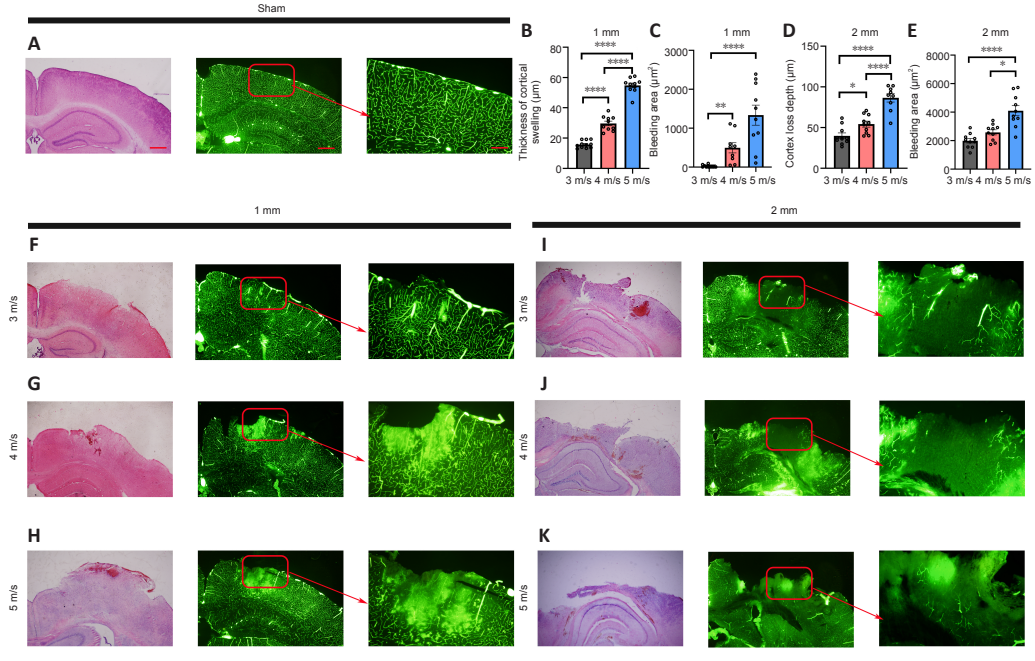

Figure 2 | **Impact of strike depth and strike speed on tissue damage.**
(A, F–K) Sham (A), 1 mm (3 m/s) (F), 1 mm (4 m/s) (G), 1 mm (5 m/s) (H), 2 mm (3 m/s) (I), 2 mm (4 m/s) (J), 2 mm (5 m/s) (K) groups. Left: HE staining (scale bars: 500 μm), middle: gelatin vascular perfusion imaging; the green fluorescence represents the vascular lumen (scale bars: 500 μm), right: enlarged image of the damaged area of gelatin vascular perfusion imaging (scale bars: 200 μm). (B, C) Cortical swelling thickness (B) and cortical hemorrhage surface (C) in the 1 mm group (n = 3 mice in each group). (D, E) Depth of cortical loss (D) and subcortical hemorrhage area (E) in the 2 mm group (n = 3 mice in each group). Data are expressed as the mean ± SEM. $^*P < 0.05$, $^{**}P < 0.01$, $^{****}P < 0.0001$ (one-way analysis of variance followed by Tukey's multiple comparisons test). HE: Hematoxylin and eosin.

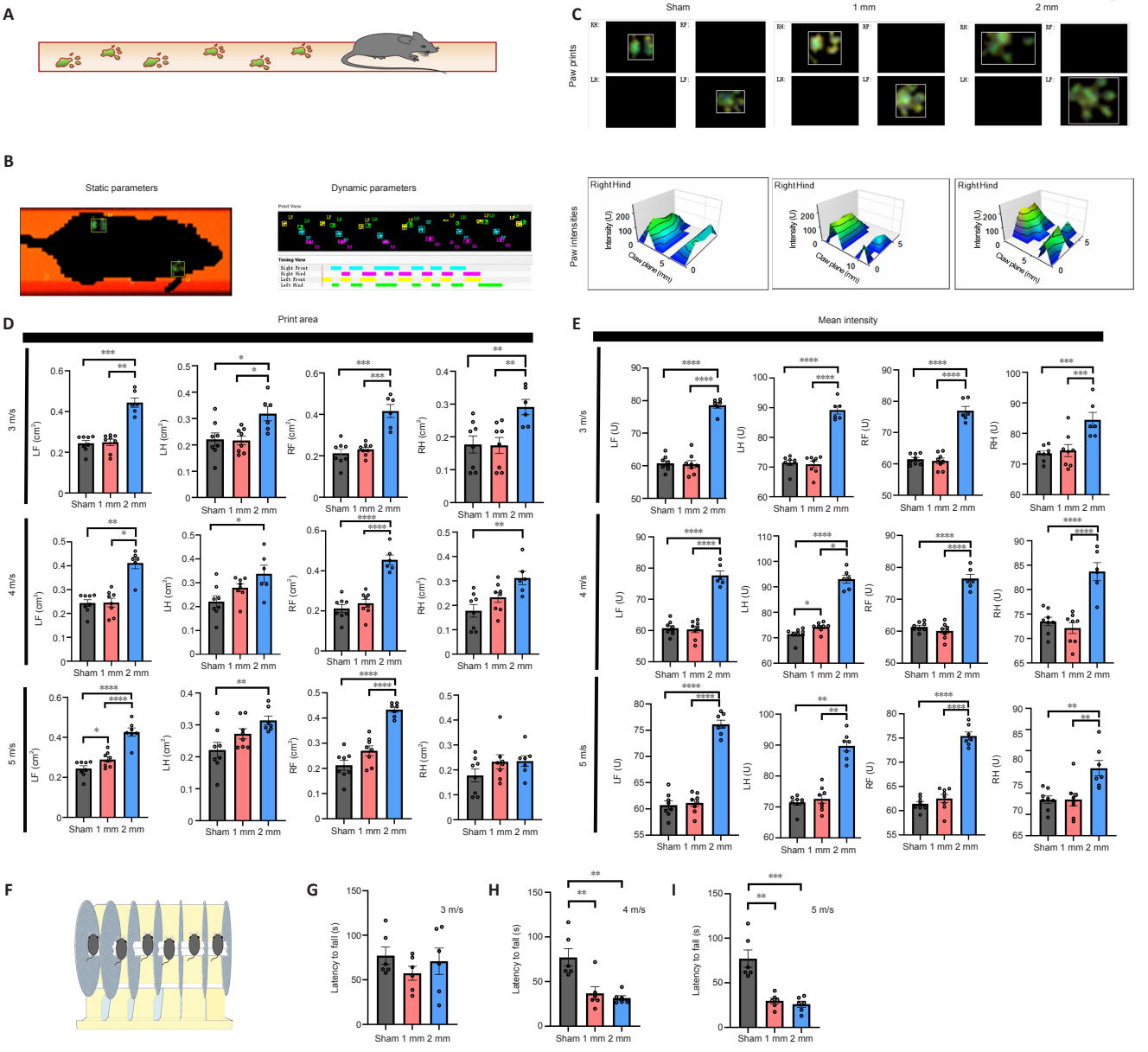

Figure 3 | **There is a significant difference in dyskinesia between the 1 and 2 mm groups on day 7 after injury.**
(A) Schematic diagram of the gait experiment. (B) Left: Schematic representation of static gait results (green indicates the print area of the claw). Right: Schematic representation of dynamic gait results. Blue: right front paw, red: right rear paw, yellow: left front paw, green: left rear paw. (C) Top: representative plot of paw print area; green indicates the print area of the claw. Bottom: representative graph of right hind paw strength; red represents higher intensity, blue represents lower intensity. (D) Paw printing area results. Left to right: left front foot, left hind foot, right front foot, and right hind foot. Top to bottom: 3, 4, and 5 m/s groups. (E) Average paw strength results. Left to right: left forefoot, left hindfoot, right forefoot, and right hindfoot. Top to bottom: 3, 4, and 5 m/s groups. Sham, n = 8; 1 mm (3 m/s), n = 8; 2 mm (3 m/s), n = 6; 1 mm (4 m/s), n = 8; 2 mm (4 m/s), n = 6; 1 mm (5 m/s), n = 8; 2 mm (5 m/s), n = 7 (mean ± SEM). (F) Schematic diagram of the rotarod experiment. (G) Rotarod test results in the sham, 1 mm (3 m/s), and 2 mm (3 m/s) groups. (H) Rotarod test results in the sham group, 1 mm (4 m/s), and 2 mm (4 m/s) groups. (I) Rotarod test results in the sham, 1 mm (5 m/s) group, and 2 mm (5 m/s) groups. n = 6 mice in each group. Data are expressed as mean ± SEM. *P < 0.05, **P < 0.01, ***P < 0.001, ****P < 0.0001 (one-way analysis of variance followed by Tukey's multiple comparisons test).

think it is necessary to more carefully divide mitochondrial subtypes, because reversible mitochondrial (normal reactive) subtypes should be the main object of rescue during the treatment of TBI.

We counted the different types of mitochondria in the 1 and 2 mm groups on days 7 and 30 and their proportion relative to the total number of mitochondria (**Figure 9A** and **G**). The normal type of mitochondria in the 1 and 2 mm groups was significantly reduced on day 7 compared with numbers in the sham group (**Figure 9B**, $P_{sham\text{-}1mm}$= 0.001; $P_{sham\text{-}2mm}$< 0.0001). The 1 mm group exhibited mostly reactive and reactive degenerate mitochondria, while 52% of the total mitochondria the 2 mm group was terminal mitochondria. On day 30, the number of normal reactive mitochondria in the sham group gradually increased and the number of reactive/degenerated mitochondria decreased. The 1 mm group showed predominantly normal reactive mitochondria, while the 2 mm group showed a significant increase in reactive/degenerated mitochondria (**Figure 9C**, P_{7d-30d}= 0.023) and decreased mitochondria at the end stage (**Figure 9D**, P_{7d-30d}= 0.015).

The main reason for different mitochondrial microstructure changes in the 1 and 2 mm groups was that the damage of normal reactive mitochondria belonged to the mitochondrial cristae swelling (**Additional Figure 15A**) and was reversible while the damage to the mitochondrial matrix vacuolation (**Additional Figure 15B**) that occurs in reactive/degenerating mitochondria was irreversible (Khmelinskii and Makarov, 2022). This may also be the reason for the difference in mitochondrial density between the 1 and 2 mm groups (**Figure 9E** and **F**). There was no significant difference in mitochondrial density between the sham, 1 mm, and 2 mm groups on day 7. After 30 days, many reactive/degenerated mitochondria and terminal mitochondria in the 2 mm group were dying, which led to a decrease in mitochondrial density in the 2 mm group; this may also be the reason for the decrease in the mitochondrial density in the 1 mm group. These findings suggest that differences in the dynamic changes of mitochondria may contribute to the difference in injury damage patterns between the 1 and 2 mm groups.

Discussion

Although researchers can precisely control the depth of injury, speed of injury, and dwell time in the CCI model compared with other modeling methods, little is known about the neuropathological damage caused by different injury parameters (Siebold et al., 2018) and there is no consensus on modeling types of RBI. Clinically, the degree of craniocerebral injury is determined by imaging

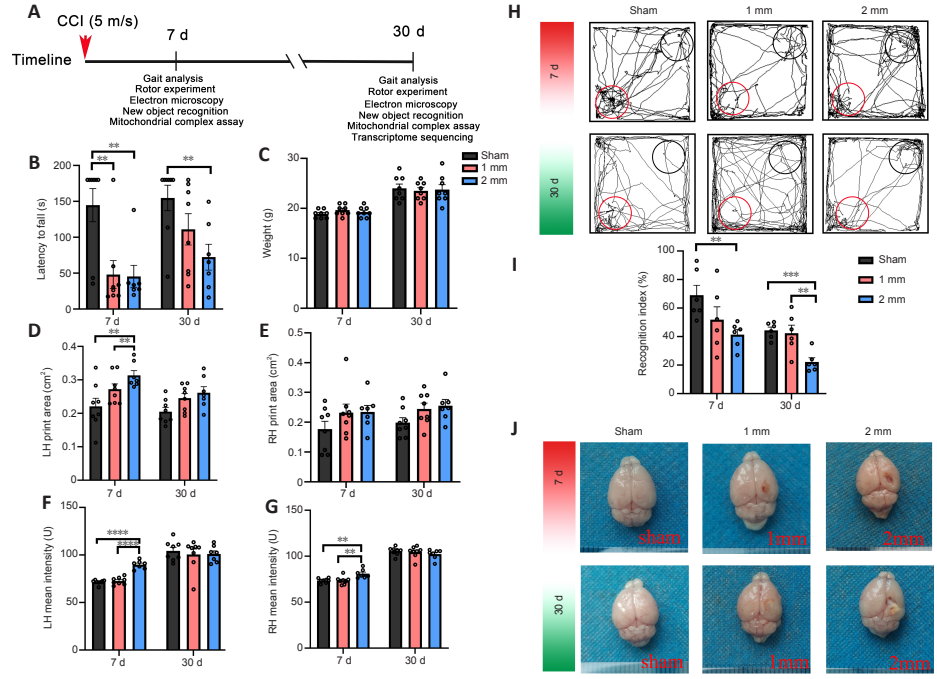

Figure 4 | Motor function and cognitive function of mice in the 1 mm group and 2 mm group at 5 m/s.
(A) Timeline of CCI modeling and experimental workflow. (B) Rotarod test results, (C) body weight, (D) left hind paw print area, (E) right hind paw area, (F) left hind paw intensity, (G) right hind paw intensity (n = 8 in each group). (H, I) Representative plots (H) and discrimination index (I) of new object recognition on days 7 and 30 after injury (n = 6 mice in each group). (J) Brain of the 1 and 2 mm groups on days 7 and 30 after injury. On day 7, the relatively complete brain tissue in the 1 mm group showed local hemorrhage, while the 2 mm group showed obvious cortical loss. On day 30, the brain tissue in the 1 mm group was intact, with local liquefaction and necrosis; in the 2 mm group, the right hemisphere was atrophied, the midline of the brain shifted to the affected side, and the brain cavity was formed. Data are expressed as mean ± SEM. $^{**}P < 0.01$, $^{***}P < 0.001$, $^{****}P < 0.0001$ (one-way analysis of variance followed by Tukey's multiple comparisons test).

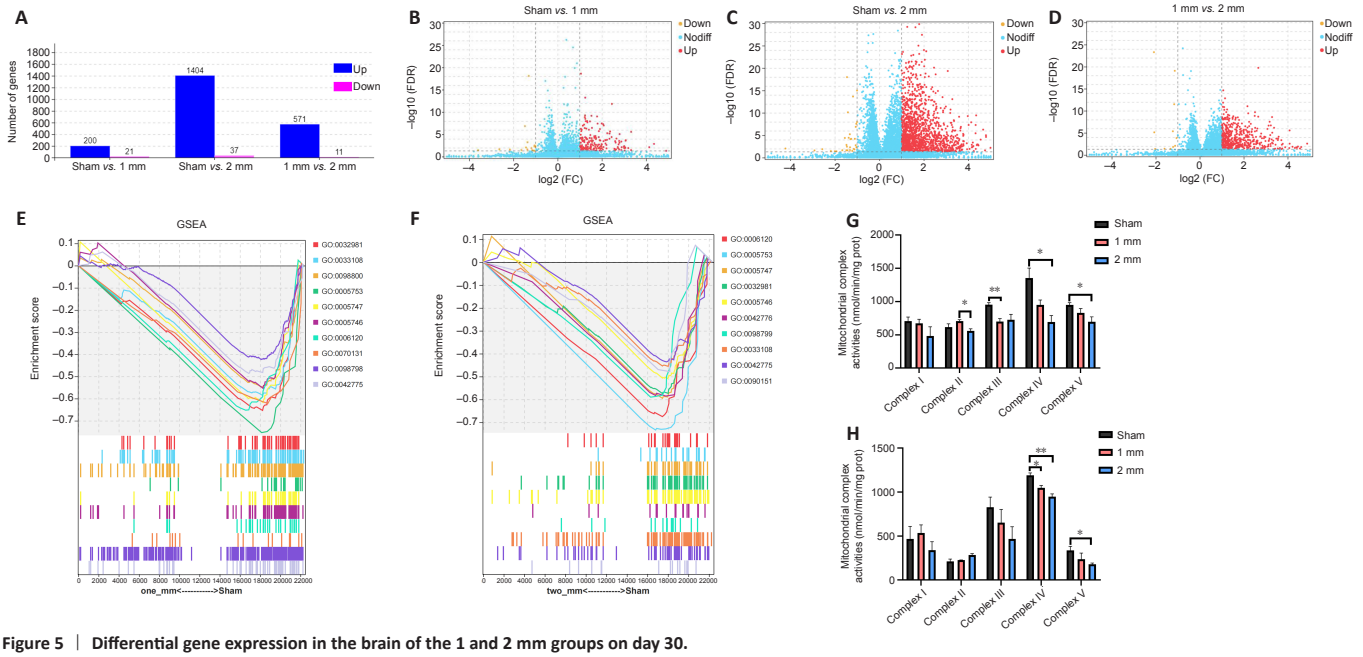

Figure 5 | Differential gene expression in the brain of the 1 and 2 mm groups on day 30.
(A) Pairwise comparison of differential gene expression between the sham, 1 mm, and 2 mm groups. (B–D) Volcano plot of differential gene expression in the 1 mm group *vs*. the sham group (B), the 2 mm group *vs*. the sham group (C), and the 2 mm group *vs*. the 1 mm group (D). (E, F) Gene Set Enrichment Analysis (GSEA) of mitochondrial-related genes in the 1 mm group *vs*. the sham group (E) and the 2 mm group *vs*. the sham group (F). (G, H) Mitochondrial complex activity in brain injury area on days 7 (G) and 30 (H) after CCI. n = 3 mice in each group. Data are expressed as mean ± SEM. $^{*}P < 0.05$, $^{**}P < 0.01$ (one-way analysis of variance followed by Tukey's multiple comparisons test). FC: Fold change; FDR: false discovery rate.

findings, duration of loss of consciousness, and Glasgow Coma Scale score, including eye and language responses (Yamamoto et al., 2018). However, these evaluation methods are not suitable for determining the degree of CCI injury in mice. Currently, most researchers use histological findings to define injury severity in mouse CCI models (Ma et al., 2019). Here, we investigated changes in cerebral blood flow, differences in the degree of cortical damage, and differences in motor function under different injury parameters of 1 and 2 mm at injury speeds of 3, 4, and 5 m/s. We also explored both the functional changes and mitochondrial damage between the 1 and 2 mm groups in the acute and chronic phases.

Our results showed that the cerebral blood flow in the injured area of the 1 mm group was significantly increased, and swelling and bulging of brain tissue, increased vascular permeability, and large-scale exudation occurred. In the 2 mm group, the main pathological changes were decreased cerebral blood flow, brain tissue loss, and cerebral vasospasm occlusion in the injured area, which existed 24 hours after injury. Thus, the degree of damage was different between the 1 and 2 mm groups. Changes in cerebral blood flow were significantly correlated with cerebral edema, cerebral hemorrhage, and other secondary brain injuries. Therefore, we believe that the detection of blood flow changes and the degree of vascular damage can be an important and effective assessment method in CCI models. The decrease of cerebral blood flow in the injured area caused by severe TBI is recognized, but there are few studies on the changes of cerebral blood flow in the injured area in the 1 mm injury model. Some researchers used a laser speckle imager to study model mice with injury parameters of 4 m/s–1.5 mm; the blood flow in the injured area decreased and then recovered, which was inconsistent with our results (Zheng et al., 2022). However, other studies have found increased blood flow in the injured area in mild TBI (Hanalioglu et al., 2022). We speculate that this may be from inconsistencies between modeling equipment, resulting in different zero calibration positions between studies.

Our results showed that compared with the 1 mm group, the 2 mm group showed gait changes on day 7 and returned to normal on day 30, suggesting the 2 mm model was severely affected in the early stage. On day 30, while gradual recovery of motor function was observed, changes in cognitive function were present in the 2 mm group, while the 1 mm group showed normal cognitive levels. In the Reactome enrichment analysis, the pathways

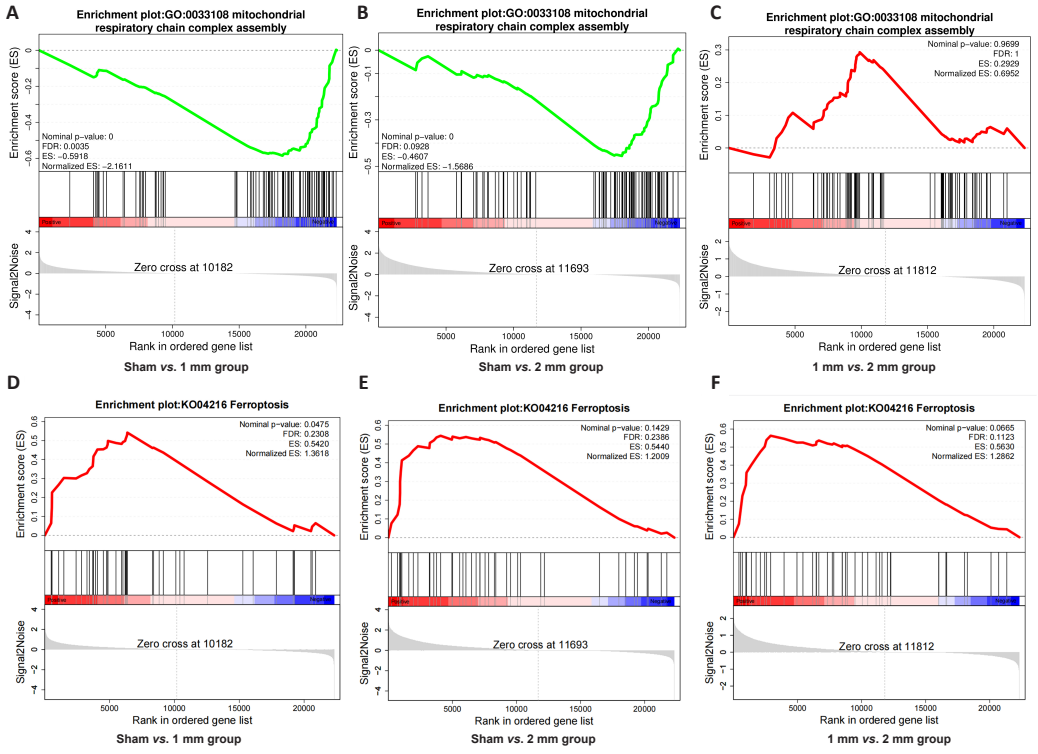

Figure 6 | Mitochondrial respiratory chain complex and ferroptosis differential gene expression in the brain in the 1 and 2 mm groups on day 30.
(A–C) Differential gene expression of mitochondrial respiratory chain complex-related genes in the 1 mm group *vs*. the sham group (A), the 2 mm group *vs*. the sham group (B), and the 2 mm group *vs*. the 1 mm group (C). (D–F) Differential expression of ferroptosis-related genes in the 1 mm group *vs*. the sham group (D), the 2 mm group *vs*. the sham group (E), and the 2 mm group *vs*. the 1 mm group (F).

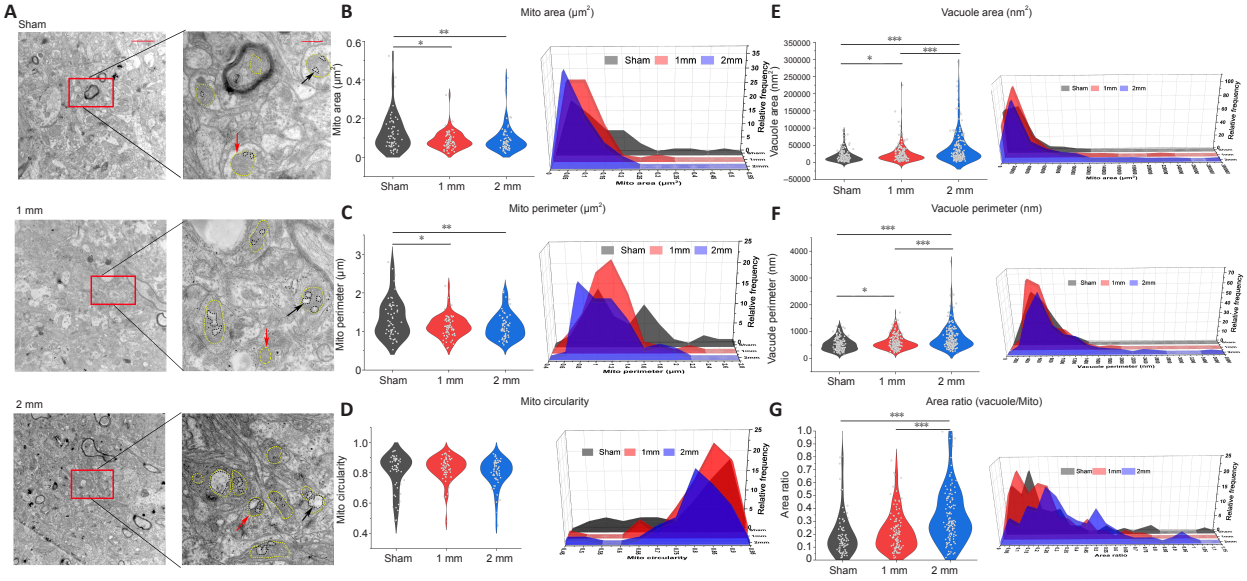

Figure 7 | Electron microscopic results of mitochondria and vacuoles in the damaged area of 1 and 2 mm groups on day 7.
(A) Mitochondria and mitochondrial vacuoles (enlarged from the boxes) in the injured brain tissue of the sham, 1 mm, and 2 mm groups. The red arrow indicates mitochondria, and the black arrow indicates vacuoles. Scale bars: 2 μm and 500 nm in the enlarged images. (B–D) Violin statistics and frequency distribution of mitochondrial area (B), mitochondrial perimeter (C), and mitochondrial circularity (D). Sham group n = 56, 1 mm group n = 72, 2 mm group n = 65. (E–G) Violin diagram and frequency distribution of vacuolar area (E), vacuolar perimeter (F), and vacuolar/mitochondrial area ratio (G). Sham group n = 160, 1 mm group n = 196, 2 mm group n = 192. n = 3 mice in each group. Data are expressed as the mean ± SEM. *P < 0.05, **P < 0.01, ***P < 0.001 (Kruskal-Wallis H test and Nemenyi multiple comparisons test).

with the most differential genes are hemostasis and apoptosis, which means that the DEGs in the 2 mm group were enriched in hemostasis and apoptosis. We thus speculate that early gait analysis and late cognitive function detection may help distinguish these two injury models.

Animal CCI models cannot fully simulate the disease status of patients with clinical craniocerebral trauma, especially because of the inconsistency of assessment methods such as modified neurological severity score or histopathological evaluation, and the current animal models do not fully correspond to patients with craniocerebral trauma. One study showed that the Disability Rating Scale at 1–4 weeks in patients with severe brain injury predicts prognosis after 6 months (Yamal et al., 2021). Another study showed that dynamic motor control index during walking cannot effectively distinguish chronic brain injury patients from healthy individuals (Acuna et al., 2022), which was consistent with our gait analysis. A study on cognitive function found that the Wechsler Memory Scale score of patients with severe brain injury was significantly lower than that of patients with moderate TBI (Carlozzi et al., 2013). Thus, cognitive function may be one of the effective ways to distinguish between moderate and severe TBI.

Impaired mitochondrial biological function and disturbances in mitochondrial dynamics are prominent features in traumatic encephalopathy, and the extent of mitochondrial dysfunction is a key determinant of neuronal survival, tissue loss, and functional recovery (Kumar Sahel et al., 2019). Multiple mechanisms are involved in mitochondrial dysfunction, such as calcium overload, oxidative stress, and glutamate excitotoxicity (Jarrahi et al., 2020). These mechanisms affect the heterogeneous mitochondrial population to varying degrees. Studies have suggested that the survival of mitochondria in damaged areas

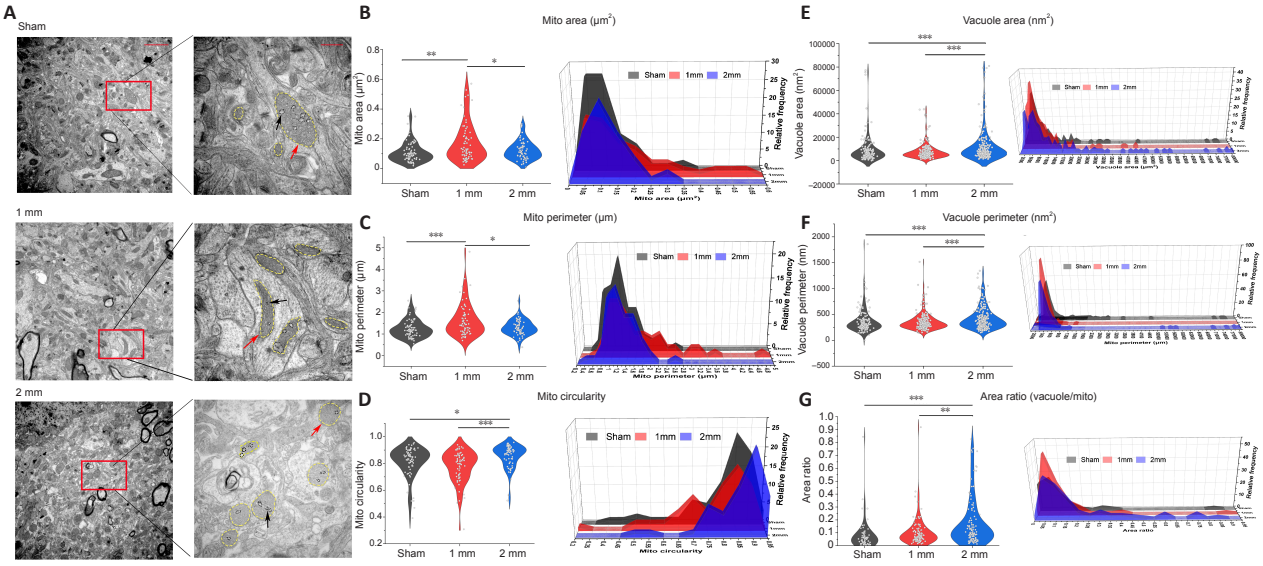

Figure 8 | **Electron microscopic results of mitochondria and vacuoles in the damaged area of 1 and 2 mm groups on day 30.**
(A) Mitochondria and mitochondrial vacuoles in the injured brain tissue of the Sham group, the 1 mm group, and the 2 mm group. The red arrow indicates mitochondria, and the black arrow indicates vacuoles. Compared with mitochondria in the Sham group and 2 mm group, mitochondria in 1 mm group were larger. Compared with mitochondria in the Sham group and 1 mm group, mitochondria in the 2 mm group became round and vacuoles became larger. Scale bars: 2 μm and 500 nm in the enlarged images. (B–D) Violin statistics and frequency distribution of mitochondrial area (B), mitochondrial perimeter (C), and mitochondrial circularity (D). Sham group n = 76, 1 mm group n = 68, 2 mm group n = 64. (E–G) Violin diagram and frequency distribution of vacuolar area (E), vacuolar perimeter (F), and vacuolar/mitochondrial area ratio (G). Sham group n = 189, 1 mm group n = 221, 2 mm group n = 217. n = 3 mice in each group. Data are expressed as mean ± SEM. *P < 0.05, **P < 0.01, ***P < 0.001 (Kruskal-Wallis H test and Nemenyi multiple comparisons test).

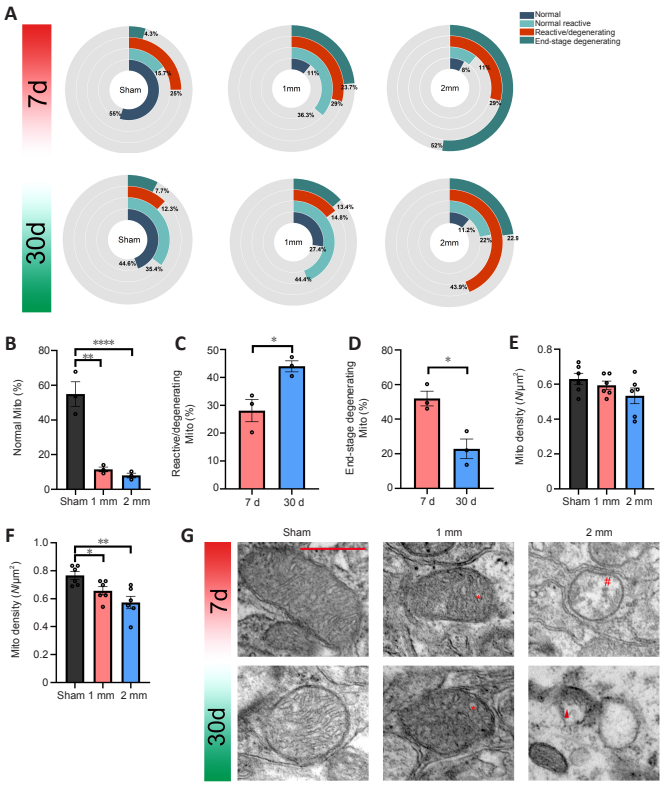

Figure 9 | **Mitochondrial density and mitochondrial damage in injured brain tissue on days 7 and 30.**
(A) Proportion of the four mitochondrial subtypes on days 7 and 30. (B) The percentage of normal mitochondria in total mitochondria on day 7. (C, D) The proportion of reactive/degenerating mitochondria (C) and proportion of end-stage degenerating mitochondria (D) in the 2 mm group on days 7 and 30. (E) Mitochondrial density in brain tissue in the injured area on day 7 (n = 3 mice in each group). (F) Mitochondrial density in brain tissue in the injured area on day 30 (n = 3 mice in each group). (G) Representative transmission electron microscope images of tissue containing the mitochondrial isoforms (scale bar: 500 nm). *Normal reactive because of swelling of mitochondrial cristae. #Mitochondrial matrix swelling leads to mitochondrial vacuolization (end-stage degenerating). ▲ Electron density is normal but membrane vesicle buds (reactive/degenerating). Data are expressed as mean ± SEM. *P < 0.05, **P < 0.01, ****P < 0.0001 (one-way analysis of variance followed by Tukey's multiple comparisons test for B, E, F; two-tailed unpaired t-test for C, D).

is a result of lower calcium ion sensitivity and reduced efficiency of calcium overload-induced swelling (Lifshitz et al., 2004). Surviving mitochondrial populations provide cells with metabolic support for survival or repair. This may be why the surviving mitochondria in the 1 mm group were enlarged on day 30. This implies the disappearance of a mitochondrial population sensitive to mitochondrial permeability transitions in part of the brain tissue in the injured area after TBI. The decrease of mitochondrial density observed by electron microscopy on day 30 in the 1 and 2 mm groups may be from the disappearance of calcium ion-sensitive mitochondria. Different pathological manifestations may lead to different mitochondrial energy metabolism patterns (Nordstrom et al., 2016). The appearance of different damage patterns in the 1 and 2 mm groups. The regulation of mitochondrial dynamics after TBI significantly improves brain edema, oxidative damage, and other damage (Salman et al., 2021), which may be the reason why the 1 and 2 mm groups show different behavioral changes on days 7 and 30. We performed transcriptome sequencing analysis of brain injury areas of mice in the 1 and 2 mm groups, and significant differences were found in mitochondria-related genes in both groups compared with the sham group. The high transcription level of ferroptosis-related genes in the injury group also attracted our attention (Geng et al., 2021). Electron microscopy showed that mitochondria became smaller and the mitochondrial membrane density increased. We evaluated the proportion of different types of mitochondria and found two different mitochondrial death/compensation patterns in the 1 and 2 mm injury models.

Intracellular energy homeostasis is maintained through a balance of mitochondria fusion and division. Under conditions of high metabolic activity or stress, mitochondria undergo fusion to increase the mitochondrial density to maximize ATP production. Fission mainly occurs in damaged cells or during apoptosis, transporting mitochondria to energy-deficient areas through division and proliferation and leading to phagocytic degradation of damaged mitochondria (Fischer et al., 2016). ROS content in the injured area of the 1 and 2 mm groups increased on day 7, and the mitochondria became smaller. We speculate that mitochondrial fission and ferroptosis may be involved in this process. We further examined ROS content and gait analysis results and found that base of support hind paws and ROS showed a significant negative correlation. This suggests that indicators of gait analysis may be used to reflect the degree of oxidative stress in brain tissue in the injured area. The fusion of mitochondria in the 1 mm group during the next 30 days may be a compensatory mechanism for surviving mitochondria. From these findings, we speculate that the response of mitochondrial damage to injury is regulated by different pathways.

Ferroptosis is a type of cell death that occurs from iron-dependent lipid peroxidation that originates from excessive accumulation of ROS (Tang et al., 2020). Elevated ROS triggers opening of the mitochondrial membrane permeability transition pore, leading to osmotic pressure imbalance and swelling of the mitochondrial matrix, disrupting the integrity of the mitochondrial outer model (Zhang et al., 2022). We detected a significant increase in ROS in the injured brain tissue of the 1 and 2 mm groups on day 7, with no significant difference between groups. The high transcription level of ferroptosis-related genes in the injury group also attracted our attention. Transcriptome sequencing revealed that both the 1 and 2 mm groups on day

30 exhibited high expression of ferroptosis-related genes, and there were significant differences between the two groups. The mechanism of the effect of ROS on ferroptosis requires further study.

Our study has some limitations. First, we chose relatively few modeling parameters; however, the seven groups of models we have explored contain the parameters used in most of the articles currently published (Siebold et al., 2018). Second, we observed mitochondria only on days 7 and 30, and we did not evaluate dynamic changes in the four types of mitochondria. Third, our study focused on the assessment of motor and cognitive abilities after CCI, but we did not analyze post-traumatic psychiatric disorders. Further research is needed to explore these issues. We have not yet further explored the functional defects of different subtypes of mitochondria and how to save mitochondrial disorders. However, our results suggest that reversible mitochondria should be specifically rescued in different degrees of brain injury models. Rational management of mitochondrial subtypes may be an important direction of treatment and nursing for patients with acute and chronic TBI.

We explored differences in terms of cerebral blood flow, brain tissue damage, motor function, and cognitive function between moderate (1 mm group) and severe CCI models (2 mm group). The results provide reliable data and evaluation methods for the further establishment of standard animal models. Additionally, significant differences in mitochondrial morphology and function were found between the 1 mm and 2 mm groups, which provides a new direction for the accurate classification of TBI.

Author contributions: *SXW, GHC and YZ designed the experiments. DDY, XDW, ADC and YFL carried out the experiments. DDY and ADC analyzed the experimental results. DDY and GHC wrote the manuscript. ZQY, JCL, JW and YZW took part in the experiments and proposed some suggestions. All authors approved the final version of this paper.*
Conflicts of interest: *The authors have no conflict of interest to declare.*
Data availability statement: *All data generated or analyzed during this study are included in this published article and its Additional files.*
Open access statement: *This is an open access journal, and articles are distributed under the terms of the Creative Commons AttributionNonCommercial-ShareAlike 4.0 License, which allows others to remix, tweak, and build upon the work non-commercially, as long as appropriate credit is given and the new creations are licensed under the identical terms.*
Additional files:
Additional Figure 1: *Cerebral blood perfusion changes in CCI model detected by laser speckle imager.*
Additional Figure 2: *Dynamic parameters of the sham, 1 mm, and 2 mm groups under the condition of 3 m/s.*
Additional Figure 3: *Paw printing results in the sham, 1 mm, and 2 mm groups under the condition of 3 m/s.*
Additional Figure 4: *The paw strength of the sham, 1 mm, and 2 mm groups under the condition of 3 m/s.*
Additional Figure 5: *Dynamic parameters of the sham, 1 mm, and 2 mm groups under the condition of 4 m/s.*
Additional Figure 6: *Paw printing results in the sham, 1 mm, and 2 mm groups under the condition of 4 m/s.*
Additional Figure 7: *The paw strength of the sham, 1 mm, and 2 mm groups under the condition of 4 m/s.*
Additional Figure 8: *Dynamic parameters of the sham, 1 mm, and 2 mm groups under the condition of 5 m/s.*
Additional Figure 9: *Paw printing results in the sham, 1 mm, and 2 mm groups under the condition of 5 m/s.*
Additional Figure 10: *The paw strength in the sham, 1 mm, and 2 mm groups under the condition of 5 m/s.*
Additional Figure 11: *Gait analysis results of the sham, 1 mm, and 2 mm groups under the condition of 5 m/s on day 30.*
Additional Figure 12: *Reactome enrichment analysis results.*
Additional Figure 13: *Representative Perl's iron staining images and MDA contents in brain tissue of the sham, 1 mm, and 2 mm groups under the condition of 5 m/s on day 30.*
Additional Figure 14: *ROS contents in the sham, 1 mm, 2 mm groups under the condition of 5 m/s on day 7.*
Additional Figure 15: *Representative transmission electron microscopic images of mitochondrial crista and mitochondrial matrix swelling.*
Additional Table 1: *Statistical strategy.*
Additional Table 2: *Data statistics details.*
Additional Table 3: *Transmission electron microscopic changes of mitochondria and vacuoles on days 7 and 30.*

References

Acuna SA, Tyler ME, Thelen DG (2022) Individuals with chronic mild-to-moderate traumatic brain injury exhibit decreased neuromuscular complexity during gait. Neurorehabil Neural Repair 36:317-327.
Al-Mufti F, Amuluru K, Changa A, Lander M, Patel N, Wajswol E, Al-Marsoummi S, Alzubaidi B, Singh IP, Nuoman R, Gandhi C (2017) Traumatic brain injury and intracranial hemorrhage-induced cerebral vasospasm: a systematic review. Neurosurg Focus 43:E14.
Anania P, Battaglini D, Miller JP, Balestrino A, Prior A, D'Andrea A, Badaloni F, Pelosi P, Robba C, Zona G, Fiaschi P (2021) Escalation therapy in severe traumatic brain injury: how long is intracranial pressure monitoring necessary? Neurosurg Rev 44:2415-2423.
Bagnato S, Boccagni C (2020) Moderate/severe traumatic brain injury as a trigger of chronic neurodegeneration in humans. Neural Regen Res 15:1247-1248.
Balan IS, Saladino AJ, Aarabi B, Castellani RJ, Wade C, Stein DM, Eisenberg HM, Chen HH, Fiskum G (2013) Cellular alterations in human traumatic brain injury: changes in mitochondrial morphology reflect regional levels of injury severity. J Neurotrauma 30:367-381.
Carlozzi NE, Grech J, Tulsky DS (2013) Memory functioning in individuals with traumatic brain injury: an examination of the Wechsler Memory Scale-Fourth Edition (WMS-IV). J Clin Exp Neuropsychol 35:906-914.
Chen ZL, Li Q, Yang JY, Yuan BQ (2022) The prevalence and risk factors of posttraumatic cerebral infarction in patients with traumatic brain injury: a systematic review and meta-analysis. Bioengineered 13:11706-11717.
Cheng H, Wang N, Ma X, Wang P, Dong W, Chen Z, Wu M, Wang Z, Wang L, Guan D, Zhao R (2022) Spatial-temporal changes of iron deposition and iron metabolism after traumatic brain injury in mice. Front Mol Neurosci 15:949573.
Dewan MC, Rattani A, Gupta S, Baticulon RE, Hung YC, Punchak M, Agrawal A, Adeleye AO, Shrime MG, Rubiano AM, Rosenfeld JV, Park KB (2018) Estimating the global incidence of traumatic brain injury. J Neurosurg:1-18.
Fischer TD, Hylin MJ, Zhao J, Moore AN, Waxham MN, Dash PK (2016) Altered mitochondrial dynamics and TBI pathophysiology. Front Syst Neurosci 10:29.
Geng Z, Guo Z, Guo R, Ye R, Zhu W, Yan B (2021) Ferroptosis and traumatic brain injury. Brain Res Bull 172:212-219.
Hakiminia B, Alikiaii B, Khorvash F, Mousavi S (2022) Oxidative stress and mitochondrial dysfunction following traumatic brain injury: From mechanistic view to targeted therapeutic opportunities. Fundam Clin Pharmacol 36:612-662.
Hanalioglu S, Hidayatov T, Isikay I, Aktas CC, Yemisci M, Mut M (2022) Early cerebral blood flow changes, cerebrovascular reactivity and cortical spreading depolarizations in experimental mild traumatic brain injury model. Turk Neurosurg 32:488-499.
Hu Y, Tao W (2021) Microenvironmental variations after blood-brain barrier breakdown in traumatic brain injury. Front Mol Neurosci 14:750810.
Hubbard WB, Joseph B, Spry M, Vekaria HJ, Saatman KE, Sullivan PG (2019) Acute mitochondrial impairment underlies prolonged cellular dysfunction after repeated mild traumatic brain injuries. J Neurotrauma 36:1252-1263.
Jarrahi A, Braun M, Ahluwalia M, Gupta RV, Wilson M, Munie S, Ahluwalia P, Vender JR, Vale FL, Dhandapani KM, Vaibhav K (2020) Revisiting traumatic brain injury: from molecular mechanisms to therapeutic interventions. Biomedicines 8:389.
Jullienne A, Obenaus A, Ichkova A, Savona-Baron C, Pearce WJ, Badaut J (2016) Chronic cerebrovascular dysfunction after traumatic brain injury. J Neurosci Res 94:609-622.
Karlander M, Ljungqvist J, Sorbo A, Zelano J (2022) Risk and cause of death in post-traumatic epilepsy: a register-based retrospective cohort study. J Neurol 269:6014-6020.
Khmelinskii I, Makarov V (2022) Theoretical analysis of reversible and irreversible mitochondrial swelling invivo. Biosystems 217:104679.
Kumar Sahel D, Kaira M, Raj K, Sharma S, Singh S (2019) Mitochondrial dysfunctioning and neuroinflammation: Recent highlights on the possible mechanisms involved in traumatic brain injury. Neurosci Lett 710:134347.
Lifshitz J, Sullivan PG, Hovda DA, Wieloch T, McIntosh TK (2004) Mitochondrial damage and dysfunction in traumatic brain injury. Mitochondrion 4:705-713.
Ma X, Aravind A, Pfister BJ, Chandra N, Haorah J (2019) Animal models of traumatic brain injury and assessment of injury severity. Mol Neurobiol 56:5332-5345.
Majdan M, Plancikova D, Brazinova A, Rusnak M, Nieboer D, Feigin V, Maas A (2016) Epidemiology of traumatic brain injuries in Europe: a cross-sectional analysis. Lancet Public Health 1:e76-83.
Moore L, Tardif PA, Lauzier F, Berube M, Archambault P, Lamontagne F, Chasse M, Stelfox HT, Gabbe B, Lecky F, Kortbeek J, Lessard Bonaventure P, Truchon C, Turgeon AF (2020) Low-value clinical practices in adult traumatic brain injury: an umbrella review. J Neurotrauma 37:2605-2615.
Mureșanu IA, Grad DA, Mureșanu DF, Hapca E, Benedek I, Jemna N, Strilciuc Ș, Popescu BO, Perju-Dumbravă L, Chereches RM (2022) The effect of cerebrolysin on anxiety, depression, and cognition in moderate and severe traumatic brain injury patients: a CAPTAIN II retrospective trial analysis. Medicina (Kaunas) 58:648.
Nordstrom CH, Nielsen TH, Schalen W, Reinstrup P, Ungerstedt U (2016) Biochemical indications of cerebral ischaemia and mitochondrial dysfunction in severe brain trauma analysed with regard to type of lesion. Acta Neurochir (Wien) 158:1231-1240.
Paxinos G, Franklin KBJ (2013) Paxinos and Franklin's the mouse brain in stereotaxic coordinates. 4th ed. Boston: Elsevier/Academic Press.
Pitzer C, Kurpiers B, Eltokhi A (2021) Gait performance of adolescent mice assessed by the CatWalk XT depends on age, strain and sex and correlates with speed and body weight. Sci Rep 11:21372.
Rubiano AM, Carney N, Chesnut R, Puyana JC (2015) Global neurotrauma research challenges and opportunities. Nature 527:S193-197.
Salman M, Kaushik P, Tabassum H, Parvez S (2021) Melatonin provides neuroprotection following traumatic brain injury-promoted mitochondrial perturbation in wistar rat. Cell Mol Neurobiol 41:765-781.
Schneider CA, Rasband WS, Eliceiri KW (2012) NIH Image to ImageJ: 25 years of image analysis. Nat Methods 9:671-675.
Siebold L, Obenaus A, Goyal R (2018) Criteria to define mild, moderate, and severe traumatic brain injury in the mouse controlled cortical impact model. Exp Neurol 310:48-57.
Sun X, Xin S, Li W, Zhang Y, Ye L (2022) Discovery of Notch pathway-related genes for predicting prognosis and tumor microenvironment status in bladder cancer. Front Genet 13:928778.
Tang S, Gao P, Chen H, Zhou X, Ou Y, He Y (2020) The role of iron, its metabolism and ferroptosis in traumatic brain injury. Front Cell Neurosci 14:590789.
Walter J, Kovalenko O, Younsi A, Grutza M, Unterberg A, Zweckberger K (2020) The CatWalk XT(R) is a valid tool for objective assessment of motor function in the acute phase after controlled cortical impact in mice. Behav Brain Res 392:112680.
Walter J, Mende J, Hutagalung S, Grutza M, Younsi A, Zheng G, Unterberg AW, Zweckberger K (2022) Focal lesion size poorly correlates with motor function after experimental traumatic brain injury in mice. PLoS One 17:e0265448.
Wang WX, Prajapati P, Vekaria HJ, Spry M, Cloud AL, Sullivan PG, Springer JE (2021) Temporal changes in inflammatory mitochondria-enriched microRNAs following traumatic brain injury and effects of miR-146a nanoparticle delivery. Neural Regen Res 16:514-522.
Xie BS, Wang YQ, Lin Y, Mao Q, Feng JF, Gao GY, Jiang JY (2019) Inhibition of ferroptosis attenuates tissue damage and improves long-term outcomes after traumatic brain injury in mice. CNS Neurosci Ther 25:465-475.
Yamal JM, Aisiku IP, Hannay HJ, Brito FA, Robertson CS (2021) Disability rating scale in the first few weeks after a severe traumatic brain injury as a predictor of 6-month functional outcome. Neurosurgery 88:619-626.
Yamamoto S, Levin HS, Prough DS (2018) Mild, moderate and severe: terminology implications for clinical and experimental traumatic brain injury. Curr Opin Neurol 31:672-680.
Yang MS, Xu XJ, Zhang B, Niu F, Liu BY (2021) Comparative transcriptomic analysis of rat versus mouse cerebral cortex after traumatic brain injury. Neural Regen Res 16:1235-1243.
Zhang P, Chen Y, Zhang S, Chen G (2022) Mitochondria-related ferroptosis drives cognitive deficits in neonatal mice following sevoflurane administration. Front Med (Lausanne) 9:887062.
Zhang YP, Cai J, Shields LB, Liu N, Xu XM, Shields CB (2014) Traumatic brain injury using mouse models. Transl Stroke Res 5:454-471.
Zheng S, Mu S, Li J, Zhang S, Wei L, Wang M, Xu Y, Wang S (2022) Cerebral venous hemodynamic responses in a mouse model of traumatic brain injury. Brain Res 1792:148014.

C-Editor: Zhao M; S-Editor: Li CH; L-Editors: Li CH, Song LP; T-Editor: Jia Y